

# THE INFLUENCE OF SPIRAL ARMS ON ACTION-BASED DYNAMICAL MILKY WAY DISK MODELLING

WILMA H. TRICK<sup>1,2</sup>, JO BOVY<sup>3</sup>, ELENA D’ONGHIA<sup>???</sup>, AND HANS-WALTER RIX<sup>1</sup>  
*Draft version June 30, 2016*

## ABSTRACT

- One sentence on what RoadMapping is.
- Overall axisymmetric RoadMapping modelling works in the presence of non-axisymmetric spiral arms, as long as spiral arms do not dominate too much.
- Our simple assumption for a DF, a single qDF, seems to be surprisingly successful in modelling the snapshot galaxy.
- Forces can be reliably recovered at the position of the stars that entered the analysis, with only small biases induced by the spiral arms.
- A survey volume of  $r_{\text{kpc}} = 3$  kpc gives equally good constraints on a spatially averaged radial and vertical forces as a volume with  $r_{\text{max}} = 5$  kpc. However, only the latter seems to be able to recover the true halo scale length.

*Keywords:* Galaxy: disk — Galaxy: fundamental parameters — Galaxy: kinematics and dynamics — Galaxy: structure — [TO DO]

## 1. INTRODUCTION

The first step in learning more about the Milky Way’s (MW) overall gravitational potential and orbit distribution function (DF)—which are crucial for understanding galaxy structure and formation—is to find the “best possible” axisymmetric model for the Galaxy. Given such a model the identification and characterization of non-axisymmetries like the bar, spiral arms or stellar streams in stellar phase-space (and chemical abundance) data would then become more straightforward.

Several approaches to constrain an axisymmetric potential and/or orbit DF have recently been put forward: Bovy & Rix (2013) and Piffl et al. (2014) fitted potential and DF simultaneously to stellar kinematics in the disk and got precise constraints on the overall potential; Sanders & Binney (2015) and Das & Binney (2016) investigated extended DFs for the disk and halo respectively (given a fiducial potential), that included in addition to the distribution in orbit space also metallicity of the star.

In this work we will continue our investigation of the RoadMapping approach (“Recovery of the Orbit Action Distribution of Mono-Abundance Populations and Potential INference for our Galaxy”). The first application of RoadMapping was done by Bovy & Rix (2013) and ?, hereafter Paper I, performed a detailed analysis of the strengths and weaknesses of the approach.

The idea behind RoadMapping is, that simple stellar populations in the MW disk—be it mono-abundance populations (???) TO DO (i.e., stars with the same [Fe/H] and [α/H] Check) or maybe also mono-age populations [References: Maybe Martig???, Any Bovy reference about age???]—follow simple orbit DFs, like, e.g.,

the quasi-isothermal DF (qDF) by ?. Given an assumed gravitational potential one can calculate the orbits—or specifically the orbit’s actions  $\mathbf{J} = (J_R, J_\phi = L_z, J_z)$ , which are integrals of motions—from the star’s current phase-space position  $(\mathbf{x}, \mathbf{v})$ . Only if the assumed gravitational potential is realistic, this orbital action distribution will follow a realistic orbit DF like the qDF. This allows one to simultaneously fit potential and orbit DF to observations.

Bovy & Rix (2013) employed this approach to measure the Milky Way’s surface density profile within 1.1 kpc using how many? MAPs in the Galactic disk from the SEGUE survey Check Reference. Their potential model had only two Check free parameters (disk scale length and halo contribution to the radial force at the solar radius). To account for missing model flexibility they constrained the surface density for each MAP only at one best radius. The profile they derived in this fashion had a scale length of  $R_s = 2.5$  kpc and was—in the regime  $R > 6$  kpc Check—later confirmed by Piffl et al. (2014) using a different action-based procedure.

Given the success of this first application and in anticipation of the upcoming data releases from Gaia in 2016–2022 Check, Trick et al. 2016 improved the RoadMapping machinery and studied its strengths and breakdowns in detail, by investigating a large suite of mock data sets. Under the prerequisite of axisymmetric data and model, they found that RoadMapping’s modelling success is stable against minor misjudgements of DF or selection function, and that—if the true potential is not contained in the proposed family of model potentials—one can still find a good fit, given the limitations of the model. Paper I also found that measurement uncertainties of the order of those by the final Gaia data release should be good enough (within 3 kpc from the Sun) to allow for precise and unbiased modelling results.

[TO DO: Continue]

What was not investigated in Paper I, was the break-

<sup>1</sup> Max-Planck-Institut für Astronomie, Königstuhl 17, D-69117 Heidelberg, Germany

<sup>2</sup> Correspondence should be addressed to trick@mpia.de.

<sup>3</sup> Department of Astronomy and Astrophysics, University of Toronto, 50 St. George Street, Toronto, ON, M5S 3H4, Canada

down of axisymmetry in the data and what would happen if both axisymmetric distribution function and potential models would therefore not contain the true DF and potential anymore. This will be this work's subject of investigation.

Here we will specifically investigate the important question, if axisymmetric *RoadMapping* modelling can still give reliable constraints on the potential in the presence of non-axisymmetric spiral arms in the data.

•

- Main question: Does axisymmetric *RoadMapping* modelling work in the presence of non-axisymmetric spiral arms?
- Consequences: Both potential and orbit DF are not axisymmetric, i.e., the fitted axisymmetric potential model and DF do per se not contain the truth.
- How to approach this: Use simulation by D'Onghia et al. 2013 and apply RM to it
- The potential model we use is chosen mostly for practical reasons and is not necessarily the optimal one for the simulation. Also, we use a single qDF as DF - because it is the simplest thing to do. Also independently of the non-axisymmetries the chosen models might deviate from the truth. Where we investigated deviations between model and truth in isolated test cases, here several assumptions break down simultaneously.
- Explain actions very shortly.  $\mathbf{J} = (J_R, J_\phi = L_z, J_z)$  quantify oscillation in the coordinate directions  $(R, \phi, z)$ . Are calculated from current phase-space position in a given potential  $\Phi$ .
- Say that actions are conserved in an axisymmetric potential, but not in non-axisymmetric potentials. (Maybe the mean vertical action is conserved [TO DO: Reference].) It is therefore important to check, if our modelling works in a system where actions are not conserved.

## 2. DATA FROM A GALAXY SIMULATION

### 2.1. Description of the galaxy simulation

In this work we use stellar phase-space data drawn from high-resolution N-body simulation snapshot of a disk galaxy by D'Onghia et al. (2013) carried out with GADGET-3 code described in Springel et al. (2005), in which overdensities with properties similar to giant molecular clouds induced prominent spiral arms—and therefore non-axisymmetric sub-structure—via the swing amplification mechanism.

For details see D'Onghia et al. (2013), here we summarize the essential characteristics.

The simulation has a gravitationally evolving stellar disk within a static/rigid analytic dark matter halo.

The analytic halo follows a Hernquist (1990) profile

$$\rho_{\text{dm}}(r) = \frac{M_{\text{dm}}}{2\pi} \frac{a_{\text{dm}}}{r(r + a_{\text{dm}})^3} \quad (1)$$

with total halo mass  $M_{\text{dm}} = 9.5 \cdot 10^{11} M_\odot$  and scale length  $a_{\text{dm}} = 29$  kpc (Elena D'Onghia, private communication). [There is no way to check that this is indeed

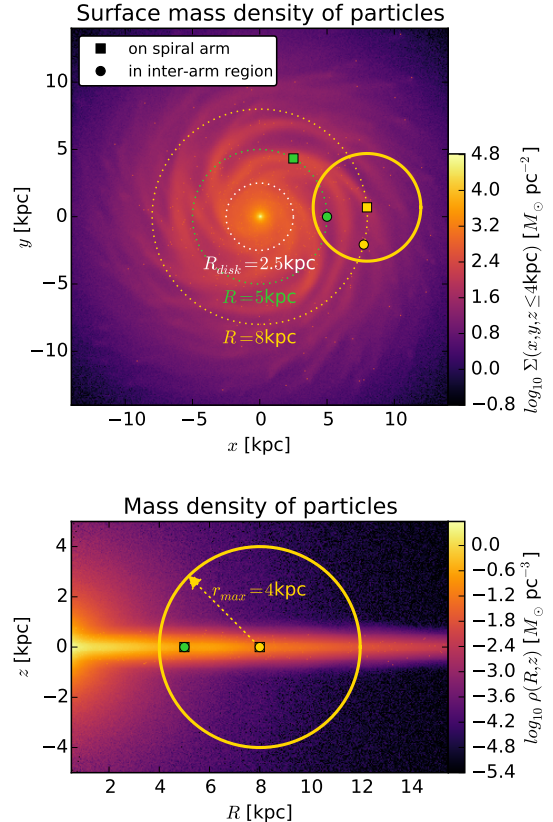


**Figure 1.** Simulation snapshot by D'Onghia et al. (2013). Shown are the surface mass density (in  $(x, y)$  plane, upper panel) and mass density (in  $(R, z)$  plane, lower panel) of the “star” particles belonging to disk, bulge and giant molecular clouds. (The dark matter halo in this simulation is static and analytic and not shown here.) Overplotted are the disk's scale length  $R_s = 2.5$  kpc (see Section 2.1) and the radii at which we center our test survey volumes in this investigation,  $R = 8$  and  $5$  kpc. The centers of the different survey volumes are marked with a square, if the survey volume is centered on a spiral arm, or with a circle, if the volume is centered on an inter-arm region. The yellow circle with radius  $r_{\text{max}} = 4$  kpc marks the survey volume in which we conduct the analysis discussed in detail in Section 4.1. [TO DO: Rename  $R_{\text{disk}}$  to  $R_s$  as it is the scale length of the disk.]

the case. What should I do?] [What does "total mass computed at 160 kpc mean? What does concentration  $c=9$  mean for a Hernquist halo? How does that fit together with  $a=29$  kpc?]

The disk consists of  $10^8$  “disk star” particles, each having a mass of  $\sim 370 M_\odot$ , and  $1000$  “giant molecular cloud” particles with mass  $\sim 9.5 \cdot 10^5 M_\odot$ . Initially the particles are distributed following an exponential disk profile with density

$$\rho_*(R, z) = \frac{M_*}{4\pi z_0 R_s^2} \text{sech}^2\left(\frac{z}{z_0}\right) \exp\left(-\frac{R}{R_s}\right),$$

with  $R_s = 2.5$  kpc and  $z_0 = 0.1R_s$  [TO DO: Check in my own measurements] and total disk mass  $M_* = 0.04 \cdot M_{\text{dm}} = 3.8 \cdot 10^{10} M_\odot$ .

The bulge consists of  $10^7$  “bulge star” particles with mass  $\sim 950 M_\odot$  and they are distributed following a spherical Hernquist profile analogous to Equation (1), with total mass  $M_{\text{bulge}} = 0.01 \cdot M_{\text{dm}} = 9.5 \cdot 10^9 M_\odot$  and scale length  $a_{\text{bulge}} = 0.1 \cdot R_s = 0.25$  kpc.

The simulation snapshot which we are using in this

work has evolved under its own gravity for  $\sim 250$  Myr, which corresponds to approximately one orbital period at  $R \sim 8$  kpc. The mass density of simulation particles (without the DM halo) at this snapshot time is shown in Figure 1. Pronounced spiral arms have developed due to the “molecular cloud perturbers”, which can be seen in Figure 1 as small overdensities in the disk. The spherical bulge and very flattened disk are shown in the lower panel in Figure 1.

We have confirmed that the gravitational center of the particles corresponds to the coordinate origin.

## 2.2. Survey volume and data

The selection function of all-sky surveys like Gaia, that are only limited by the brightness of the tracers, are contiguous and—when ignoring anisotropic effects like dust obscuration—spherical in shape. For simplicity we will use spherical survey volumes centered on different vantage points and with sharp edges at a radius  $r_{\max}$  around it (see also Section 3.1), which corresponds to a magnitude cut for stellar tracers all having the same luminosity. Figure 1 illustrates the different survey volume positions we use in this study: We use each a volume with  $r_{\max} = 1, 2, 3, 4$  or  $5$  kpc centered on a spiral arm and on an inter-arm region at both the equivalent of the solar radius in this simulation,  $R = 8$  kpc, and at  $R = 5$  kpc, where the spiral arms are more pronounced (see Figure [TO DO: Make plot that illustrates strength of spiral arm and reference it here]) than at  $R = 8$  kpc. From each volume we draw  $N_* = 20,000$  random “disk star” particles from the simulation and use their phase-space positions ( $\mathbf{x}_i, \mathbf{v}_i$ ) within the simulated galaxy’s restframe as data. To make the data sample more realistic, one would actually have to add measurement uncertainties, especially to the distances of the survey volumes central vantage point and the proper motions measured from there. We decided not to include measurement uncertainties: Firstly, their effect on *RoadMapping* modelling has been already investigated in Paper I and we found that the measurement uncertainties of the last data release of Gaia should be small enough to not disturb the modelling to much. Secondly, in this study we want to isolate and investigate the deviations of the data from the assumed potential and DF model and axisymmetry independently of other effect.

## 2.3. Symmetrized potential model

For a galaxy with pronounced spiral arms an axisymmetric model matter distribution can per se not reproduce the true matter distribution globally. We derived an *overall best fit symmetrized* potential model from the distribution of particles to be able (i) to quantify the non-axisymmetries in the simulation snapshot better and (ii) to compare how close our axisymmetric *RoadMapping* results can get to it.

We derive this model by fitting axisymmetric analytical functions to the density distribution of each of the galaxy component’s particles: The bulge and halo follow each a Hernquist profile by construction (see Section [TO DO]). The disk with its spiral arms however does deviate strongly from its initial conditions in Equation ????. We chose the double exponential disk model from the *galpy* (galaxy python) library to fit the particle distribution

**Table 1**  
Best fit parameters of the DEHH-Pot (see Section [TO DO]), which we use as the global best fit symmetrized potential model.

circular velocity	$v_{\text{circ}}(R_\odot)$	$222 \text{ km s}^{-1}$
disk scale length	$h_r$	$2.5 \text{ kpc}$
disk scale height	$h_z$	$0.17 \text{ kpc}$
halo fraction	$f_{\text{halo}}$	$0.54$
halo scale length	$a_{\text{halo}}$	$29 \text{ kpc}$
bulge fraction	[TO DO]	[TO DO]
bulge scale length	[TO DO]	[TO DO]

in the disk. (This profile is better than the Miyamoto-Nagai disk in reproducing the overall radial density slope, but as it has not the advantage of allowing fast force calculations, we are not using it in the *RoadMapping* modelling.) The best fit parameters for this reference potential, to which we will refer as the **DEHH-Potential** (Double-Exponential disk + Hernquist halo + Hernquist bulge) in the remainder in this work, are given in Table [TO DO]. As can be seen in Figures [TO DO] in Section [TO DO] below, the DEHH-Pot fits the overall density distribution very well. Its density profile might be a little stepper around  $z \sim 0$  than the actual particle distribution, but this should not affect the overall discussion, as the radial density, surface density and disk-to-halo ratio profiles are so well reproduced.

Globally our *RoadMapping* model can not be better than this *overall best fit symmetrized* DEHH-Pot, which acts therefore like a global upper limit to *RoadMapping*. We note that in deriving the DEHH-Pot we used the correct decomposition into bulge, disk and halo components, while *RoadMapping* only feels the composite gravitational effect. Given the flexibility of the potential model MNHH-Pot used in *RoadMapping* and the restriction of the modelling to a survey volume, it could however be possible that *RoadMapping* can do better in fitting the local potential inside the survey volume at the price of recovering the global potential parameters to less accuracy. We will discuss this in the following sections.

## 2.4. Quantifying influence of spiral arm

[TO DO: There is a short comment on that in D’Onghia 2013 as well]

[TO DO: Maybe give the different survey centroids names A,B,C,D, so it’s easier to talk about them.]

Depending on size and position of the survey volume the spiral arms and inter-arm regions dominate the stellar distribution within the survey volume to different degrees. To quantify the strength of the spiral arm, we introduce the quantity

$$\kappa(x_j, y_j) \equiv \frac{\Sigma_{\text{disk},T}(x_j, y_j \mid |z| \leq 1.5 \text{ kpc})}{\Sigma_{\text{disk},S}(x_j, y_j \mid |z| \leq 1.5 \text{ kpc})} - 1$$

where  $\Sigma_{\text{disk},i}$  is the surface density of the disk component of the simulation snapshot ( $i = T$ ) or of the symmetrized snapshot model DEHH-Pot in Section 2.3 ( $i = S$ ) within the survey volume,

$$\Sigma_{\text{disk},i} \equiv \int_{-1.5 \text{ kpc}}^{1.5 \text{ kpc}} \rho_{\text{disk},i}(x_j, y_j, z) \, dz. \quad (2)$$

$(x_j, y_j)$  is the centroid of a surface area element  $(x_j \pm \delta, y_j \pm \delta)$  with  $\delta = 0.25$  kpc.  $(x_c, y_c, z_c = 0)$  is the posi-

tion of the survey volume's center within the simulation's cartesian coordinate system,  $c \in \{A, B, C, D\}$ . We consider all  $n \simeq \pi r_{\max}^2 / 4\delta^2$  values of  $\kappa(x_j, y_j)$  inside a given survey volume and calculate the statistics

$$\langle \kappa(r \leq r_{\max} | c) \rangle \equiv \frac{1}{n} \sum_j^n \kappa(x_j, y_j)$$

$$\text{and } \Delta\kappa(r \leq r_{\max} | c) \equiv \max[\kappa(r \leq r_{\max} | c)] - \min(r \leq r_{\max} | c)] \\ \text{with } (x_j - x_c)^2 + (y_j - y_c)^2 \leq r_{\max}.$$

This gives us information if a spiral arm or an inter-arm region dominates the survey volume ( $\langle \kappa \rangle > 0$  for spiral arms,  $\langle \kappa \rangle < 0$  for inter-arm regions) and how large the contrast between spiral arms and inter-arm regions is ( $\Delta\kappa$ ).

### 3. ROADMAPPING MODELLING

#### 3.1. Likelihood

The data that goes into the modelling are the 6D position and velocity coordinates  $(\mathbf{x}_i, \mathbf{v}_i)$  of  $N_*$  stars within the survey volume. For simplicity we use a purely spatial selection function  $\text{sf}(\mathbf{x})$  of spherical shape,

$$\text{sf}(\mathbf{x}) \equiv \begin{cases} 1 & \text{if } |\mathbf{x} - \mathbf{x}_0| \leq r_{\max} \\ 0 & \text{otherwise} \end{cases},$$

whose maximum radius  $r_{\max}$  defines the boundary of the survey volume and which is centred on  $\mathbf{x}_0 \equiv (R_0, \phi_0, z_0 = 0)$ . Given a parametrized potential model  $\Phi(R, z)$  with parameters  $p_\Phi$ , the  $i$ -th star is on an orbit characterized by the orbital actions

$$\mathbf{J}_i \equiv \mathbf{J}[\mathbf{x}_i, \mathbf{v}_i | p_\Phi].$$

The probability of stars to be on the orbit  $\mathbf{J}_i$  is proportional to a given orbit distribution function  $\text{df}(\mathbf{J})$  with parameters  $p_{\text{DF}}$ ,

$$\text{df}(\mathbf{J}_i | p_{\text{DF}}) \equiv \text{df}(\mathbf{J}[\mathbf{x}_i, \mathbf{v}_i | p_\Phi] | p_{\text{DF}}) \equiv \text{df}(\mathbf{x}_i, \mathbf{v}_i | p_\Phi, p_{\text{DF}}),$$

where the latter equivalence arises from the Jacobian determinant between the angle-action coordinates  $(\boldsymbol{\theta}, \mathbf{J})$  and cartesian phase-space coordinates  $(\mathbf{x}, \mathbf{v})$ , which is  $|\partial(\mathbf{x}, \mathbf{v})/\partial(\boldsymbol{\theta}, \mathbf{J})| = 1$  and therefore allows us to treat the  $\text{df}$  equivalently as a distribution of current phase-space coordinates or a distribution of orbital actions only, with uniform distribution in the angles  $\boldsymbol{\theta}$ . In some sense, the  $\text{df}(\mathbf{J})$  describes how we expect a realistic stellar population in the MW disk to look like.

The joint likelihood of the  $i$ -th star being on an orbit  $\mathbf{J}$  in the potential  $\Phi$  and being within the survey volume is therefore

$$\mathcal{L}_i \equiv \mathcal{L}(\mathbf{x}_i, \mathbf{v}_i) = \frac{\text{df}(\mathbf{x}_i, \mathbf{v}_i | p_\Phi, p_{\text{DF}}) \cdot \text{sf}(\mathbf{x}_i)}{\int \text{df}(\mathbf{x}, \mathbf{v} | p_\Phi, p_{\text{DF}}) \cdot \text{sf}(\mathbf{x}) d^3x d^3v}.$$

The details how we evaluate the likelihood normalisation numerically to sufficiently high enough precision are discussed in Paper I.<sup>4</sup>

In the scenario considered in this paper it can happen that there are a few ( $\sim 1$  in 20,000) stars entering the catalogue that are for some reason on rather extreme

<sup>4</sup> [TO DO: Write what exact numerical accuracy we use and check that it is actually good enough.]

orbits, e.g., moving radially directly towards the center. These kinds of orbits do not belong to the set of orbits that we classically expect to make up a overall smooth galactic disk. To avoid that such single stars with very low likelihood mess up the modelling we introduce here a simple outlier model,

$$\mathcal{L}_i \longrightarrow \max(\mathcal{L}_i, \epsilon \cdot \text{median}(\mathcal{L})),$$

where  $\epsilon = 0.001$  for  $N_* = 20,000$  stars and  $\text{median}(\mathcal{L})$  is the median of all the  $N_*$  stellar likelihoods  $\mathcal{L}_i$  with the given  $p_\Phi$  and  $p_{\text{DF}}$ . This outlier model was not used in Paper I.

Following Paper I, we assume for now uninformative flat priors on the model parameters  $p_\Phi$  and  $p_{\text{DF}}$  and find the maximum and width of the posterior probability function

$$\text{pdf}(p_\Phi, p_{\text{DF}} | \text{data}) \propto \prod_{i=1}^{N_*} \mathcal{L}_i \cdot \text{prior}(p_\Phi, p_{\text{DF}})$$

using a nested-grid approach and then explore the full shape of the  $\text{pdf}$  using a Monte Carlo Markov Chain (MCMC)<sup>5</sup>. Full details on this procedure are given in Paper I.

#### 3.2. DF model

The most simple orbit distribution function exhibiting a disk-like structure may be the quasi-isothermal distribution function (qDF) introduced by Binney (2010) and Binney & McMillan (2011). It proved to be a successful model to describe the orbit distribution of individual mono-abundance populations (MAPs) in the Galactic disk (Bovy & Rix 2013; Ting et al. 2013), that seem to be isothermal in  $z$ -direction (i.e., “quasi-isothermal”). Modelling approaches trying to capture the overall disk distribution (Piffl et al. 2014; Sanders & Binney 2015) were describing the Galactic disk as a superposition of many qDFs. The qDF, which we already used in Paper I, has the functional form

$$\text{qDF}(\mathbf{J} | p_{\text{DF}}) = f_{\sigma_R}(J_R, L_z | p_{\text{DF}}) \times f_{\sigma_z}(J_z, L_z | p_{\text{DF}}) \quad (3)$$

where

$$f_{\sigma_R}(J_R, L_z | p_{\text{DF}}) = n \times \frac{\Omega}{\pi \sigma_R^2(R_g) \kappa} \exp\left(-\frac{\kappa J_R}{\sigma_R^2(R_g)}\right) \times [1 + \tanh(L_z/L_0)] \quad (4)$$

$$f_{\sigma_z}(J_z, L_z | p_{\text{DF}}) = \frac{\nu}{2\pi \sigma_z^2(R_g)} \exp\left(-\frac{\nu J_z}{\sigma_z^2(R_g)}\right) \quad (5)$$

(Binney & McMillan 2011). The guiding-center radius  $R_g$ , circular frequency  $\Omega$ , radial/epicycle frequency  $\kappa$  and vertical frequency  $\nu$  describe the near-circular orbit with given angular momentum  $L_z$  in a given potential. Counter-rotating orbits with  $L_z < L_0$  are suppressed by the term  $[1 + \tanh(L_z/L_0)]$  (with  $L_0 \sim 10 \text{ km s}^{-1} \text{ kpc}$ ). We set the radial stellar tracer density  $n(R_g)$  and velocity

<sup>5</sup> [TO DO: Reference emcee]

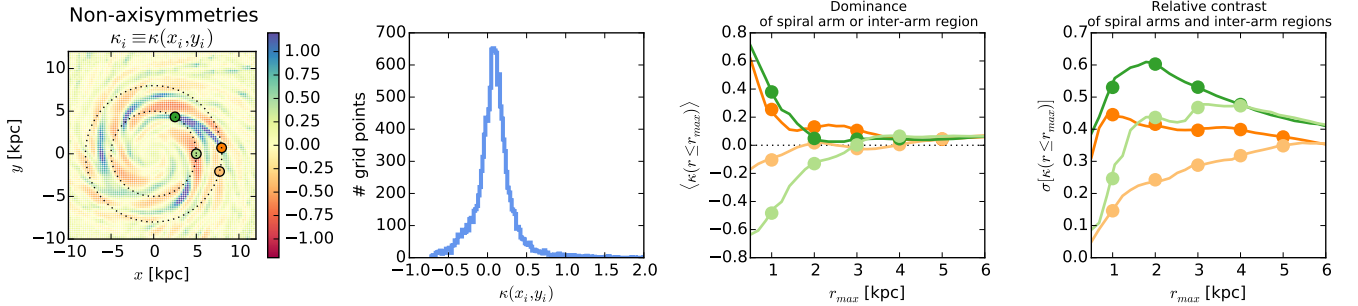


**Figure 2.** Contrast and dominance of the spiral arms. The left panel shows the values of  $\kappa_i$  calculated according to Equation [TO DO] as described in Section [TO DO] at regular grid points  $(x_i, y_i)$  with bin width 0.25 kpc. Marked are the centroids of the four test survey volumes of this study. The second panel shows a histogram over all  $\kappa(x_i, y_i)$  values in the region  $x, y \in [-14, 14]$  kpc. The two right panels show the dominance (with the mean  $\langle \kappa(r \leq r_{\max}) \rangle$  of all grid points within the survey volume as measure) and the relative contrast (with the standard deviation  $\sigma[\kappa(r \leq r_{\max})]$  as measure) of spiral arms and inter-arm regions inside a spherical survey volume with given centroid (colour-coded) and size (radius  $r_{\max}$  shown on the  $x$ -axis). We chose two volumes in which the spiral arms dominate, and two in which an inter-arm region dominates. The dominance and contrast of spiral arms and inter-arm regions is stronger at  $R = 5$  kpc than at  $R = 8$  kpc. Also, inter-arm regions appear larger and smoother than spiral arms, as already inside a small volume centred on a spiral arm the contrast is quite large. The larger the volume the more does the overall effect of spiral arms and inter-arm regions average out.

dispersion profiles  $\sigma_z(R_g)$  and  $\sigma_R(R_g)$  to

$$n(R_g | p_{\text{DF}}) \propto \exp\left(-\frac{R_g}{h_R}\right) \quad (6)$$

$$\sigma_R(R_g | p_{\text{DF}}) = \sigma_{R,0} \times \exp\left(-\frac{R_g - R_\odot}{h_{\sigma,R}}\right) \quad (7)$$

$$\sigma_z(R_g | p_{\text{DF}}) = \sigma_{z,0} \times \exp\left(-\frac{R_g - R_\odot}{h_{\sigma,z}}\right). \quad (8)$$

The free model parameters of the qDF are therefore

$$p_{\text{DF}} \equiv \{\ln h_R, \ln \sigma_{R,0}, \ln \sigma_{z,0}, h_{\sigma,R}, h_{\sigma,z}\}.$$

Even though we do not have any stellar abundance or age information in the simulation snapshot we are going to investigate (see Section 2) and we therefore cannot define stellar sub-populations for which the assumption of such a simple model might be reasonable, we will still try to model the whole disk with a single qDF—to see how far we can get with the simplest possible model.

### 3.3. Potential model

#### [TO DO]

- Introduce MNHH potential model, explain that form of disk was mostly chosen to the closed form expression of  $\Phi$  which allows for fast calculation.
- Mention action calculation and that we tested explicitly that fixing Delta=0.45 and using staeckel interpolation grid does not degrade the analysis
- Mention and reference galpy.

## 4. RESULTS

### 4.1. A single application of RoadMapping

In this section we will discuss the results of the *RoadMapping* analysis of a single data set. This fiducial data set has  $N_* = 20,000$  stars that were drawn from the spherical volume with  $r_{\max} = 4$  kpc centered on a spiral arm at the “solar” radius  $R = 8$  kpc shown as yellow sphere in Figure 1. We use *RoadMapping* to fit a single qDF (see Section [TO DO]) and the potential

model consisting of a Miyamoto-Nagai disk, a Hernquist halo and a (fixed) Hernquist bulge introduced in Section [TO DO] to it.

#### 4.1.1. Recovering the stellar distribution

In Figure 3 we compare the phase-space distribution of the 20,000 stars that entered the *RoadMapping* analysis as data with the best-fit stellar distribution, which is given by the action-based qDF and potential model found with *RoadMapping*. We note that the spiral arms introduce very strong non-axisymmetries in the data, both in the spatial and the velocity distribution (especially in  $v_R$ , where a lot more stars move outside than inside as compared to an axisymmetric model). We therefore compare in Figure 3 the data and fit separately for different spatial regions,  $R >$  and  $< 8$  kpc and  $\phi <$  and  $> 5^\circ$ . In the region where the spiral arm dominates (blue) the best fit *RoadMapping* model is actually a very poor model. However, what the model underestimates in the spiral arm, it slightly overestimates in the other regions and is therefore indeed something like a good average model for the overall distribution. Especially the region at  $R > 8$  kpc and  $\phi < 5^\circ$ , where neither the spiral arm nor the inter-arm regions dominate strongly, is extremely well described by the model. This is remarkable because we had no indication beforehand that a single qDF might be at all a good enough model to describe the overall stellar distribution in the simulation snapshot. But it obviously does—apart from the spiral arm of course, which we had no chance to capture anyway.

#### 4.1.2. Recovering the potential

As shown in the previous section the best fit *RoadMapping* model seems to reproduce the stellar phase-space distribution quite well. But is the corresponding potential close to the true potential?

Figures [TO DO] compare the true simulation snapshot potential and the axisymmetric DEHH-Pot from Table 1 with the best fit MNHH-Pot from the *RoadMapping* analysis. In particular, Figure [TO DO] illustrates the overall matter density distribution, Figure [TO DO] the rotation curve, surface density profile and disk-to-halo ratio and

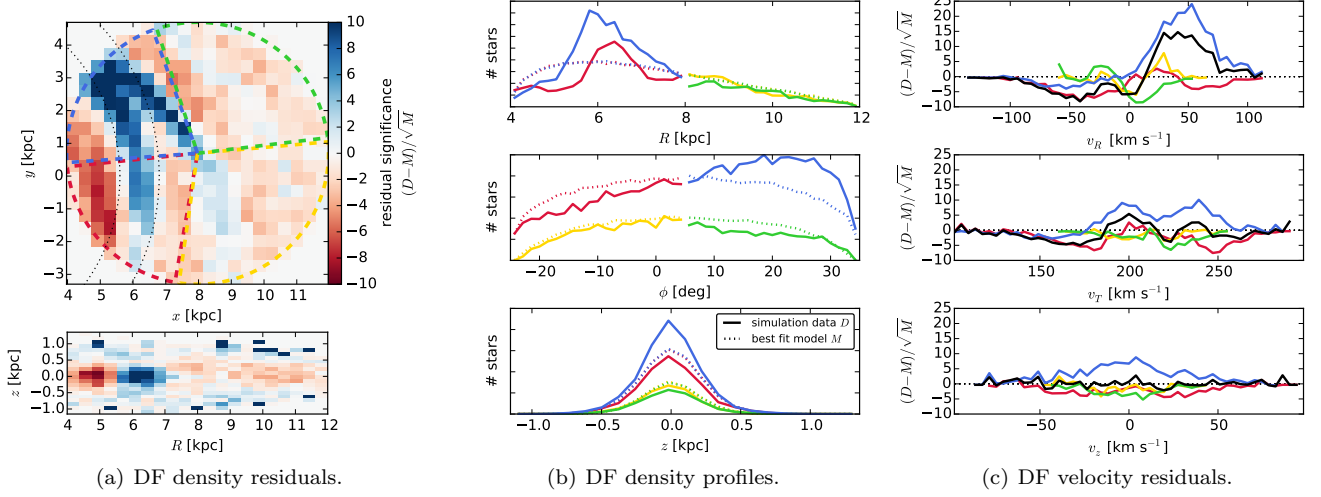


**Figure 3.** Comparison of the DF of stars in position-velocity space in the data set with  $N_* = 20,000$  and  $r_{\max} = 4$  kpc from the simulation snapshot and in the single-qDF best fit *RoadMapping* model from Section [TO DO]. Panel 3(a) shows the spatial density residual significance projected to the  $(x, y)$  and  $(R, z)$  plane. In the  $(x, y)$  panel the following regions are marked:  $R < 8$  kpc,  $\phi > 5^\circ$  (blue),  $R < 8$  kpc,  $\phi < 5^\circ$  (red),  $R > 8$  kpc,  $\phi > 5^\circ$  (green),  $R > 8$  kpc,  $\phi < 5^\circ$  (yellow). Panels 3(b) and 3(c) show the density profiles and velocity residual significance along each of the 6D phase-space coordinates separately for each of the four spatial regions. The blue region is very much dominated by the non-axisymmetric spiral arm. For the yellow region the axisymmetric single-qDF model is a good description. Overall the qDF is a good average axisymmetric model for the data. [TO DO: Move legend to R panel and make it bigger]

Figure [TO DO] compares the true and recovered gravitational forces at the position of each star in the data set.

The recovery of density, surface density and disk-to-halo ratio is especially good in the region where most of the stars are located, around  $R \sim 6$  kpc and in the plane of the disk. In large regions inside the survey volume, and even outside, the density is recovered to within 15%. Due to the spiral arms in the disk plane at smaller radii, and a misjudgement of the radial density profile at larger radii, which is most likely due to the choice of a disk potential that cannot reproduce the actual profile, The circular velocity curve is even recovered within 5% [TO DO: Check that this is also the case if we use the true rotation curve.].

- As can be seen in Figure 6 the model is a good average model for the majority of stars, i.e. in the wide inter-arm regions and also the stars the peaks of the spiral arms. For the wings of the spiral arms the model is less good: in the leading side of the spiral arm the  $|F_{R,M}|$  is underestimated because it does not account for the additional pull of the spiral arm, while in the trailing side of the spiral arm  $|F_{R,M}|$  is overestimated, as it does not feel the pull away from the Galactic center by the spiral arm.

#### 4.1.3. Recovering the action distribution

- Figure: residuals in action space, comparison of true/symmetrized vs. best fit actions (maybe also true vs. best fit in symmetrized potential), overplot  $L_z = v_{\text{circ}} * R_g$  of spiral arms

#### 4.2. The influence of spiral arms on RoadMapping

In the previous section we showed that for a large enough survey volume ( $r_{\max} = 4$  kpc) the *RoadMapping* modelling result was a good fit to the data and gave constraints on the gravitational potential which were very

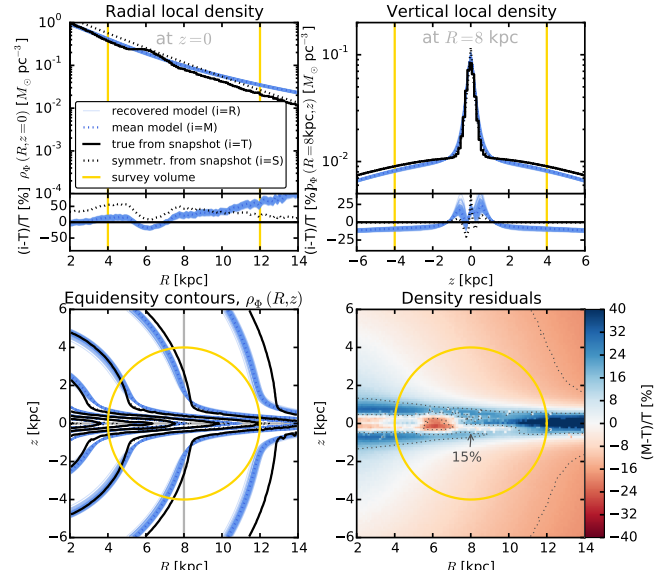


**Figure 4.** Comparison of the true density distribution  $\rho_{\Phi,T}$  in the galaxy simulation snapshot (solid black line, averaged over  $\phi$ ) with the axisymmetric density distribution  $\rho_{\Phi,R}$  recovered with *RoadMapping* (solid blue lines) from  $N_* = 20,000$  stars in the survey volume with  $r_{\max} = 4$  kpc (yellow line), as described in Section [TO DO]. The first two panels show density profiles along  $(R, z = 0)$  and  $(R = 8 \text{ kpc}, z)$ , together with the relative differences between true and recovered  $\rho_{\Phi}$ . The third panel displays equidenity contours of the matter distribution in the  $(R, z)$  plane. Overplotted are also the overall axisymmetric DEHH-Pot's  $\rho_{\Phi,S}$  (dotted black line) (see Section 2.3) and the  $\rho_{\Phi,M}$  of the recovered mean model in Table [TO DO] (dotted blue line). The last panel shows the relative difference between the true  $\rho_{\Phi,T}$  (averaged over all  $\phi$ ) and the recovered mean model  $\rho_{\Phi,M}$ . Over wide areas even outside of the survey volume the relative difference is less than 15%. At  $R \gtrsim 8$  kpc and  $z \sim 0$  it becomes apparent that the chosen potential model cannot perfectly capture the structure of the disk. [TO DO: Maybe show the profiles not at  $R=8$  and  $z=0$ , but at  $R=6$  and  $z=h_z$  or so.] TO DO: Redo plot. Now I use the median of MCMC samples as best fit model.]

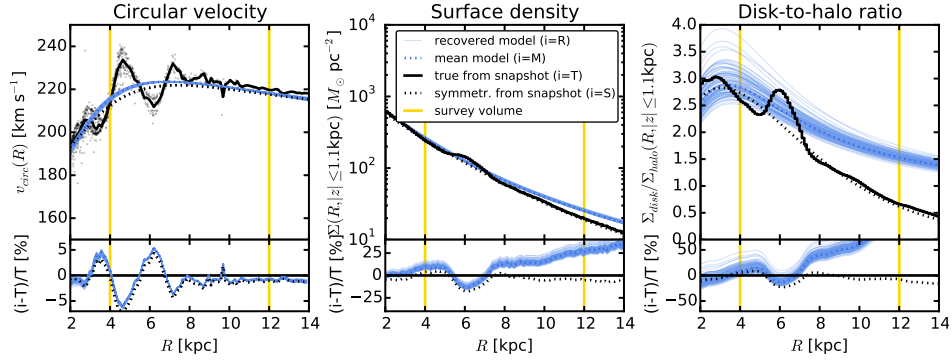


**Figure 5.** [TO DO: Remove MNHH symmetric potential from caption.] Comparison of the circular velocity curve, surface density profile within  $|z| \leq 1.1$  kpc and disk-to-halo ratio of the surface density along  $R$  for the true potential of the galaxy simulation snapshot (solid black line) and the axisymmetric model potential recovered with *RoadMapping* (solid blue lines) (see Section [TO DO]). Overplotted are also the profiles of the symmetrized "true potential" (dotted black line) (see Section [TO DO] and Table 1) and the recovered mean model (dotted blue line) (see Table [TO DO]). The circular velocity curve is recovered to less than 5%, especially at larger radii. For the surface density and disk-to-halo ratio *RoadMapping* recovers the truth at radii  $\lesssim 8$  kpc. The deviations at larger radii are connected to the discrepancies in the density in Figure [TO DO]. [TO DO: When I have the force I can probably also calculate the true circular velocity curve!] TO DO: Redo plot. Now I use the median of MCMC samples as best fit model.]

close to the true potential. In the following we want to investigate how this modelling success depends on the position and the size of the survey volume.

#### 4.2.1. Test suite and parameter recovery

We center our test survey volumes at the positions marked in Figures [TO DO] and consider volume sizes with  $r_{\text{max}} \in [0, 1, 2, 3, 4, 5]$  kpc for  $R_0 = 8$  kpc and  $r_{\text{max}} \in [0, 1, 2, 3, 4]$  kpc for  $R_0 = 5$  kpc. As demonstrated in Figure [TO DO] the spiral arm strength is very different in these four different test volumes. Each data set contains then  $N_* = 20,000$  stars inside this spherical volume and we fit a single qDF and MNHH-Pot to it. Figure 8 shows the best fit parameters for the different *RoadMapping* analyses. We also overplot the parameter of the reference DEHH-Pot in Table 1. Overall the statistical random errors on the parameter recovery are very small for  $N_* = 20,000$  and possible systematic errors dominate. Let's first consider the parameters of the gravitational potential: All volumes recover  $v_{\text{circ}}(R_\odot)$  within a few km s\$^{-1}\$; in the largest volumes, where the circular velocity curve is probed over several kpc the estimate is the most accurate. The halo fraction  $f_{\text{halo}}$  of the radial force at the Sun is very well recovered, independent of the size of the volume. The estimate that we get for the best fit Miyamoto-Nagai disk scale height  $b_{\text{disk}}$  seems to be approximately independent of the size of the volume as well. We can even recover the true halo scale length  $a_{\text{disk}}$ , however only for a volume as large as  $r_{\text{max}} = 5$  kpc. Smaller volumes that underestimate  $a_{\text{halo}}$  get slightly larger estimates for the disk scale length  $a_{\text{disk}}$  and the overall radial density slope is then probably closer to the truth, even if the individual parameters are not. [TO DO: Discuss qDF parameters.]

- at  $R=5$  is and in spiral arms is the velocity dispersion larger than at  $R=8$  and in inter-arm regions respectively.
- In small volumes the volumes with spiral arms have shorter tracer scale lengths than the volumes centered on inter-arm regions

#### 4.2.2. Size of survey volume

##### [To Do: Introductory paragraph.]

- The first and most important thing to notice is, that we get very close to recovering the true forces at the positions of the stars in the survey volume, no matter how large the survey volume is.
- The second thing to notice is, that, if we consider not the stars inside the survey volume, but a spatial average of the forces in a large volume ( $r_{\text{max}} = 5$  kpc) independent of the survey volume, the radial forces are overall very well recovered, especially for large survey volumes. There is however a overestimation of  $\sim 5 - 20\%$  in the vertical forces (depending on volume size and position) which is induced by the spiral arms (see explanation below).
- The third thing to notice is that the constraints we get on the spatially averaged forces inside  $r < 5$  kpc is almost as good for the survey volume of  $r_{\text{max}} = 3$  kpc as compared to survey volumes of  $r_{\text{max}} = 4$  or 5 kpc. If we had to decide between a  $r_{\text{max}} = 3$  kpc volume with good data quality and a larger volume with worse data quality, we would loose nothing in terms of force recovery when using the smaller volume. (Only the halo scale length might not be as well constrained, see Figure 8).
- Now let's discuss the reason for the biases that we observe. The peak of the distribution in  $\Delta F_R(*_i)$  and  $\Delta F_R(g_j)$  is slightly biased towards an underestimation of  $|F_{R,M}|$  in our *RoadMapping* models. We think the explanation is the following: Spiral arms are very thin. If a spiral arm crosses the observation volume both its leading side (at large radii) and its trailing side (at small radii) are also in the volume. Stars in the trailing side feel a lower gravitational pull towards the galaxy center than they would if there was no spiral arm. Because there are in general more stars at smaller radii, the *RoadMapping* fit is slightly biased to reproduce in general slightly weaker radial forces. [TO DO: Not

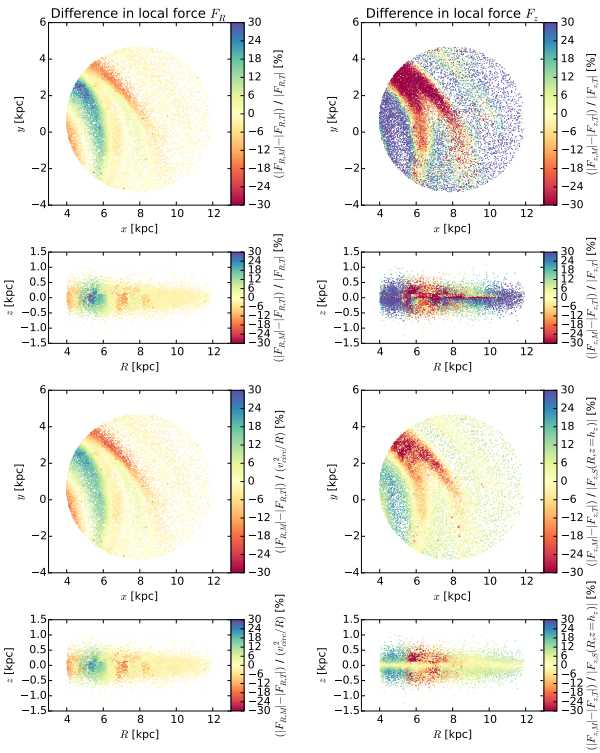


**Figure 6.** [TO DO: Rewrite. Figure was replaced.] Comparison of radial and vertical forces  $F_R = -\partial\Phi/\partial R$  and  $F_z = -\partial\Phi/\partial z$  of the true (upper two rows) or symmetrized (lower three rows, black and orange dotted lines) potential of the galaxy simulation snapshot with the potential model recovered with *RoadMapping* (solid blue lines in lower three rows). The upper two rows show the relative difference between the true potential force at the position of each star that entered the *RoadMapping* analysis, and the recovered potential force. The lower three rows compare contours of equal force and force profiles along lines of constant  $R$  and  $z$ . Overall the radial forces are very well recovered, which is related to the well recovery of the circular velocity curve in Figure ???. There are more problems with the vertical force, which is related to the higher surface densities in spiral arms and lower surface density in inter-arm regions, for which the axisymmetric model can only give a average solution. Also, the potential model is not the optimal model to describe the vertical density profile, which becomes also visible in the recovery of the vertical force close to the plane of the disk. [TO DO: Might be, that I have to re-calculate the forces for some of the stars. Write Test that tests if force  $\gtrsim 10^{10}$  and then recalculates those forces.] [TO DO: Show only the lower panels.] TO DO: Redo plot. Now I use the median of MCMC samples as best fit model.]

100% sure but it could be that, when I include the true circular velocity in the vcirc plot above, that one sees that the true vcirc (and therefore FR) is slightly larger than the recovered vcirc.]

- The peak of  $\Delta F_z(*_i)$  is approximately at 0, while the peak of  $\Delta F_z(g_j)$  is strongly biased towards an overestimation of  $|F_{z,M}|$ . There are much more stars in the spiral arms than in the inter-arm regions, and the stars in the spiral arm feel stronger vertical forces because of the higher disk mass. *RoadMapping* finds a model that in general has much stronger vertical forces than expected for a smooth potential. While the actual vertical forces that the many stars in the spiral arms feel are very well recovered, it becomes obvious when looking at the grid points regularly distributed in space

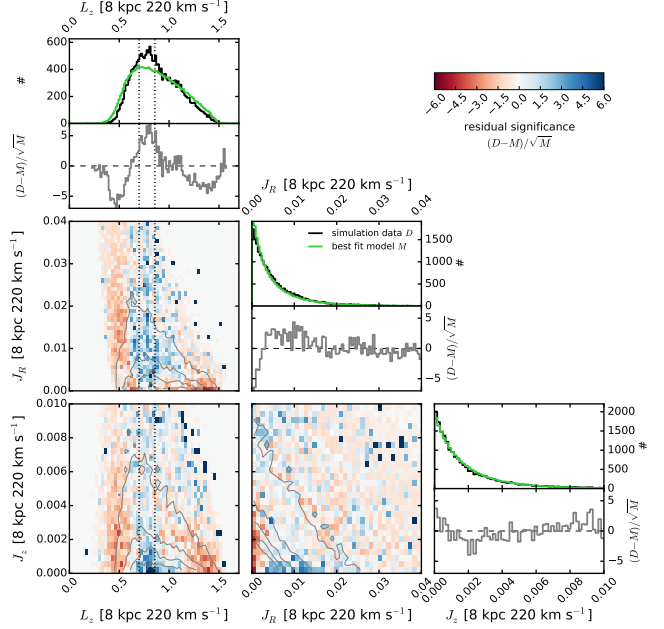


**Figure 7.** [TO DO] [TO DO: Calculate reference data new. Now I use the median of MCMC samples as best fit model.] TO DO: Redo plot. Now I use the median of MCMC samples as best fit model.]

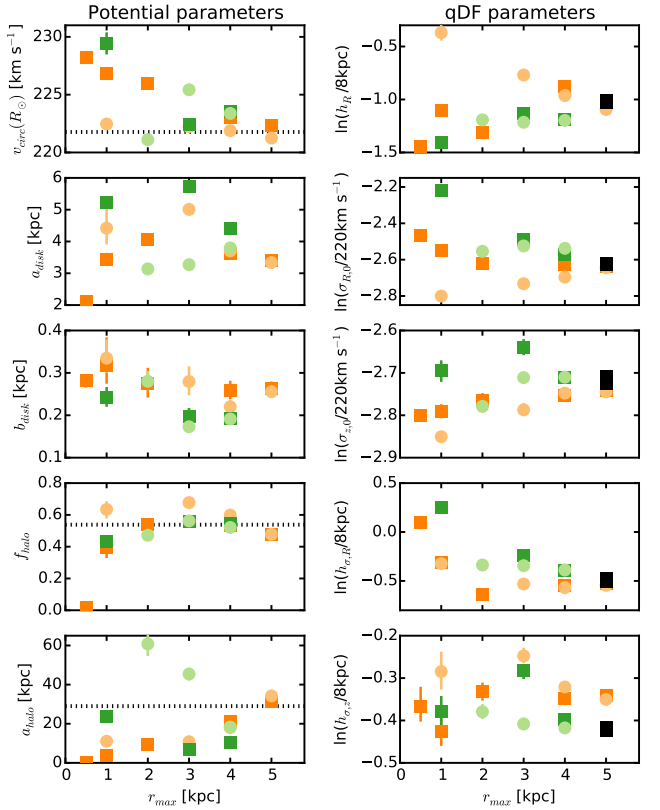


**Figure 8.** TO DO: Preliminary. Add more results. Make sure that the "true" potential parameters are the final version.

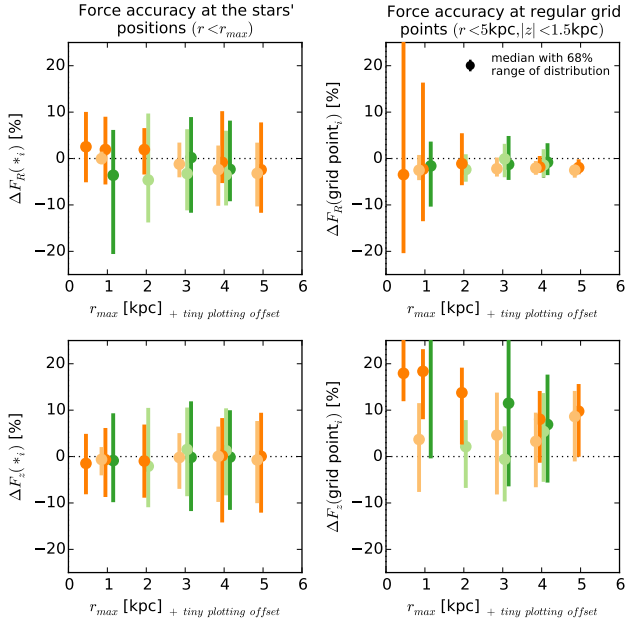


**Figure 9.** TO DO [TO DO: Make sure all final analyses are in this plot.]

that the *RoadMapping* vertical forces are much stronger. As expected the overestimation is especially strong ( $\sim 20\%$ ) for small survey volumes dominated by spiral arms, while small volumes dominated by an inter-arm region result in much better estimates for the spatially averaged  $F_z(g_j)$  ( $\sim 5\%$  bias). Large volumes lie somewhere in between (bias of  $\sim 10\%$ ).

- Because the stellar number asymmetry in the trailing vs. leading sides of spiral arms is much smaller than the stellar number asymmetry in spiral arm vs. inter-arm region, the bias is visible in the distribution of  $\Delta F_{R*}*_i$  ( $F_R$  recovery biased only by a few

stars  $\rightarrow$  bias for majority of stars visible) and not in  $\Delta F_z(*_i)$  (majority of stars biases the fit  $\rightarrow$  we recover  $F_z$  for the majority of stars), but becomes really pronounced for  $\Delta F_z g_i$  (the inter-arm regions dominate when averaging spatially  $\rightarrow$  large overestimation of  $F_z$ ) and stays small for  $\Delta F_R g_i$  (trailing and leading sides of spiral arms are similarly important when averaging spatially  $\rightarrow$  it becomes visible that the bias is actually not that big).

[TO DO: make consistent:  $i$  counts stars,  $j$  counts grid points.]

#### 4.2.3. Influence of spiral arms

- Figure: x-axis:  $\langle \kappa \rangle$ , y-axis: one panel with mean stellar rms deviation in FR and one with  $F_z$ . Analyses with same potential but at different positions and sizes within the galaxy.
- Figure: x-axis:  $\sigma_\kappa$ , y-axis: same as above figure.

## 5. SUMMARY AND CONCLUSION

### REFERENCES

- Binney, J. 2010, MNRAS, 401, 2318  
 Binney, J., & McMillan, P. 2011, MNRAS, 413, 1889  
 Bovy, J., & Rix, H.-W. 2013, ApJ, 779, 115  
 Das, P., & Binney, J. 2016, MNRAS, arXiv:1603.09332  
 D’Onghia, E., Vogelsberger, M., & Hernquist, L. 2013, ApJ, 766, 34  
 Hernquist, L. 1990, ApJ, 356, 359  
 Piffl, T., Binney, J., McMillan, P. J., et al. 2014, MNRAS, 445, 3133  
 Sanders, J. L., & Binney, J. 2015, MNRAS, 449, 3479  
 Springel, V., Di Matteo, T., & Hernquist, L. 2005, MNRAS, 361, 776  
 Ting, Y.-S., Rix, H.-W., Bovy, J., & van de Ven, G. 2013, MNRAS, 434, 652